Results in Engineering 25 (2025) 103456

Contents lists available at ScienceDirect

Results in Engineering

journal homepage: www.sciencedirect.com/journal/results-in-engineering

Research paper

Performance optimizing of pneumatic soft robotic hands using wave-shaped contour actuator

Hui Chen [a], Mohammed A.H. Ali [a,*], Zhenya Wang [b,*], Junlong Chen [c], Montaser N.A. Ramadan [a], Mohammad Alkhedher [d]

[a] Department of Mechanical Engineering, Faculty of Engineering, University of Malaya, Kuala Lumpur 50603, Malaysia
[b] Department of Mechanical Engineering, Tsinghua University, Beijing 100084, China
[c] Faculty of Engineering, School of Electrical and Computer Engineering, The University of Sydney, Camperdown/Darlington, Sydney, Australia
[d] Mechanical and Industrial Engineering Department, Abu Dhabi University, Zayed City, Abu Dhabi 59911, United Arab Emirates

ARTICLE INFO

Keywords:
Soft robotic surface
Pneumatic gripper
Wave-Shaped contour actuators
Soft robotics
Yeoh model

ABSTRACT

Soft robotic hands have gained significant attention in recent years due to their simplicity in control, ease of fabrication, and remarkable compliance. However, traditional designs often suffer from limited contact area and insufficient grasping force. In this study, we propose a novel four-finger pneumatic soft robotic hand with wave-shaped contour actuators to address these issues. Inspired by natural grasping mechanisms, the proposed design integrates multiple actuation modes to enhance both adaptability and reliability. An analytical model based on constant curvature bending theory and the Yeoh constitutive model is developed to guide the design and predict the performance of the actuators. The model is validated through extensive Abaqus finite element simulations, demonstrating excellent agreement with experimental results. Our findings confirm that the actuators achieve consistent and reliable bending motion with optimal structural parameters. Experimental evaluation of the soft robotic hand includes bending trajectory analysis and grasping tests with various irregular objects. The results show that the actuators provide a maximum bending angle of 180° under 26 kPa pressure and maintain stable grasps for objects of different shapes and sizes. The soft robotic hand demonstrates superior grasping adaptability and reliability due to its high compliance and optimized design. This study paves the way for practical applications in industrial automation, medical devices, and service robotics, highlighting the potential of wave-shaped contour actuators in enhancing the functionality of soft robotic hands.

1. Instruction

Soft robotics has emerged as a highly interdisciplinary field with extensive applications in various domains such as industrial production, medical devices, aerospace, high-pressure environments, and defense. [1–9]. While traditional robotic hands made of rigid materials have efficiently replaced humans in monotonous and repetitive tasks on production lines, improving accuracy and efficiency [10]. However, limitations become evident as the scope of robotic applications broadens [11]. As robots are deployed in more diverse and dynamic environments, the range of objects they need to handle expands, revealing the inadequacies of rigid robotic grippers [12],. Traditional rigid-structured robots struggle to provide the interactive experience required for various applications, highlighting the need for more adaptable and versatile solutions.

In order to gain insight into the multidisciplinary intersection, a variety of bionic robots have been developed by combining bionics, novel materials, new processing technologies, and intelligent control methods [13–17],. In comparison to rigid manipulators, soft manipulators are characterized by the dominance of flexible materials, with their motion generated by the deformation of these materials [18,19],. Consequently, soft manipulators demonstrate a high degree of flexibility when grasping flexible and fragile objects, and they exhibit good adaptability and safe interactivity in addressing the interaction problems of service robots. Furthermore, its applications have been extended to medical settings, as well as to service, detection, and rescue operations [18,20,21],.Recent advancements in soft robotics have led to the development of novel materials, including high-strength biodegradable polymers and self-healing elastomers, which offer enhanced durability and environmental benefits [22–25]. Studies have also introduced

* Corresponding authors.
E-mail addresses: hashem@um.edu.my (M.A.H. Ali), wangzhenya@mail.tsinghua.edu.cn (Z. Wang).

https://doi.org/10.1016/j.rineng.2024.103456
Received 17 September 2024; Received in revised form 2 November 2024; Accepted 18 November 2024
Available online 9 December 2024

hybrid driving methods, such as pneumatic-electric actuators that combine the high responsiveness of electric drives with the adaptability of pneumatic systems [26–28]. Additionally, innovative applications of soft robotics in the medical field—such as soft exoskeletons for patient rehabilitation—demonstrate the expanding capabilities of these technologies in providing effective, patient-friendly solutions [29–32]. These advancements represent significant steps forward in realizing more practical and adaptable soft robotic system.

Currently, the main driving structures for achieving motion in pneumatic soft actuators include shape-constrained driving structures, fiber-reinforced driving structures, and mesh-reinforced driving structures [2,33]. The shape-constrained structure uses deformation from differences between upper and lower chambers to achieve bending, mimicking human hand functionality. [34–39] By optimizing chamber thickness and material layout, this structure significantly reduces driving pressure and improves response speed, as exemplified by the FPN structure's excellent bending and mechanical performance [40–50].. The fiber-reinforced structure embeds fibers wound at specific angles within a silicone base to achieve predetermined motion trajectories, enhancing flexibility and allowing precise control over extension, bending, and twisting motions [51–54]..This makes it suitable for simulating various complex actions [55–59]. The mesh-reinforced structure uses special weaving techniques, combining materials like silicone and nylon mesh with varying elasticity and stiffness to regulate mechanical output [60–62]. This structure is particularly suitable for medical assistive devices, providing the necessary support and strength to aid patients in rehabilitation exercises. The proposed wave-shaped contour actuator represents an innovative approach that addresses limitations present in traditional pneumatic actuators, including limited adaptability, reduced contact stability, and insufficient grasping efficiency. The wave-shaped contour is inspired by natural geometries that enhance engagement during deformation, leading to improved adaptability and stability during grasping operations. Unlike traditional flat or straight-sidewall designs, the waveform profile provides a greater contact area, which helps in maintaining stable grasping forces, even under uneven load distribution. This is particularly useful in scenarios requiring adaptable and precise manipulation, such as handling irregularly shaped or delicate objects.

Previous studies on pneumatic soft actuators have significantly advanced their development and application in various fields. However, there are still several limitations and research gaps that need to be addressed. Many existing designs feature complex structures, which complicate fabrication and increase production costs. Additionally, traditional soft actuators often suffer from limited contact area with objects, leading to unreliable grasping performance due to position errors, fabrication inaccuracies, and installation inconsistencies. Most pneumatic actuators also typically offer only a single mode of operation, such as bending or twisting, which reduces their adaptability and flexibility in handling objects of varying shapes and stiffness [63]. To address these issues, our work proposes a novel wave-shaped contour soft actuator integrated with a four-finger pneumatic soft robotic hand. This design combines the benefits of multiple actuation modes, enhancing both the grasping adaptability and reliability of pneumatic soft actuators. By optimizing structural parameters and utilizing advanced materials, our approach aims to provide a more efficient, versatile, and robust solution for soft robotic applications, paving the way for broader and more practical uses.

In this article, the design and fabrication of the wave-shaped contour single-finger soft actuator are introduced. The detailed structure and working mechanism are explained, including comparisons with traditional FPN actuators. The kinematic and mathematical models of the actuator are then established, utilizing constant curvature bending theory and the Yeoh constitutive model to describe its behavior under various pressures. Abaqus finite element simulations are conducted to analyze stress distribution and the impact of structural parameters on bending performance. Subsequently, experiments are conducted to validate the simulation results and evaluate the actuator's bending trajectory and grasping capabilities. Finally, a series of grasping experiments involving various irregular objects are performed to demonstrate the practicality and versatility of the four-finger soft robotic hand in handling everyday items.

2. Methodology

2.1. Soft fingers design and working mechanism

2.1.1. Design of the soft finger

As illustrated in Fig. 1, the thesis presents multi-chamber flexible pneumatic soft actuator network-type actuator, constructed using a variety of super elastic silicone materials of differing qualities as the base material. The soft body actuator finger comprises an upper elastic extension layer and a lower non-expandable but flexible restriction layer. The upper layer is composed of top and side walls that enclose multiple chambers, including eight uniform chambers and a larger chamber at the finger end. The thickness of the sidewalls of the finger-end chamber is greater than that of the remaining uniform chambers. Additionally, waveform tooth profiles are incorporated into the sidewalls of each chamber, with adjacent chambers formed by sidewalls (i.e., connecting walls). At the base of the upper chamber, an air intake channel is located. The finger end of the soft body drive is designed with a flange mechanism, which serves to facilitate fixation with the base.

2.1.2. Comparison with traditional FPN actuators

Traditional FPN (Fast Pneumatic Network) multi-chamber actuators are characterized by top layers consisting of top and side walls, where the sidewalls are thinner than the top walls. The sidewalls, which connect adjacent chambers, have the least stiffness, resulting in initial bending occurring at these points. Unlike other pneumatic networks that achieve bending through the overall expansion of the top layer, the FPN's extended sidewalls enable the structure to bend more quickly, endure higher air pressures, and achieve greater bending angles.

However, the FPN design must account for the coupling effect between the sidewalls and the applied air pressure. The sidewall structure introduces gaps between chambers, which reduce the actuator's expansion efficiency and overall stiffness, subsequently diminishing the fingertip contact force. To address these challenges, this paper offers a detailed analysis.

Given the narrow airways and thin non-expandable layer, it is assumed that the deformation of the connecting walls and non-expandable layer is comparable. As shown in Fig. 2, let the length of the connecting wall be l_1, the intersection point of the perpendicular lines at both ends be O,the convergence angle be σ, and the radius of curvature be r. Based on bending stress analysis, the following relation is obtained:

$$\frac{l}{r} = \frac{|M|}{EI} \tag{1}$$

$$\delta = \frac{\gamma}{l} \tag{2}$$

Where M is the bending moment, E is the elastic modulus of the soft material, and I is the moment of inertia of the cross-sectional neutral axis.

From Eqs. (1) and (2), the following relation is obtained::

$$K = \frac{1}{\delta l} = \frac{M}{EI} \tag{3}$$

Where K is the bending stiffness, which is constant if the material and area remain unchanged. For the same bending angle, the following relation is obtained::

$$|M| \propto \frac{\gamma}{l} \tag{4}$$

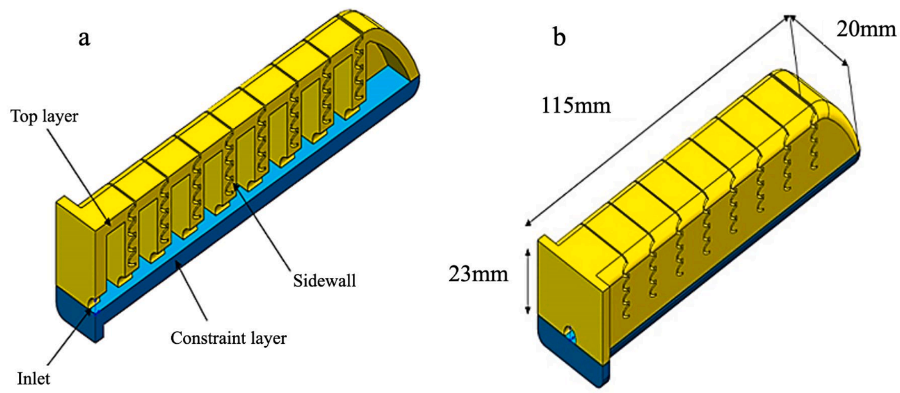

Fig. 1. Single actuator model (a) Section view, (b) Whole view.

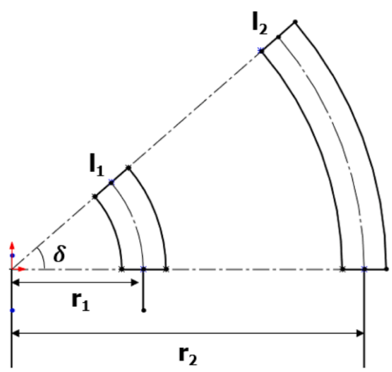

Fig. 2. Geometric schematic of single finger bending.

According to Eq. (4), while the traditional FPN structure enables rapid bending of the soft actuator, increasing the length amplifies the bending moment, making the movement between chambers more challenging. The FPN design must take into account the coupling effect between the connecting wall length and air pressure. Simulations indicate that the sidewall has the least stiffness, and directly applying the FPN structure to pneumatic soft robotic hands results in reduced expansion efficiency and diminished gripping force due to this low stiffness.

To address these limitations, this paper introduces a wave-shaped contour soft actuator, as illustrated in Fig. 1. Unlike traditional FPN multi-chamber pneumatic soft actuators, the sidewalls of the proposed actuator feature wave-shaped contours. During expansion, these contours between adjacent chambers engage smoothly, ensuring quick and uninterrupted interaction. This design enhances contact between chambers, reduces gaps without altering finger length, and ultimately provides greater fingertip output force and improved bending performance. The physical structure parameters of the soft actuator are detailed in Table 1.

2.2. Kinematic and mathematical modelling of single-finger actuators

Flexible actuators capable of large deformations, such as pneumatic soft actuators, frequently utilize constant curvature bending theory to address movement challenges. [64] By modeling the bending motion of the soft actuator as constant curvature bending, the kinematic model and mathematical matrix are simplified, effectively linking the actuator's motion characteristics, geometric parameters, and bending performance.

Table 1
Geometric parameters of the single-finger actuator.

Parameter	Value(mm)(mm)
Length l_0	115
Number of Chambers	8
Wall Thickness n	1.5
Constraint Layer Thickness	3

2.2.1. Kinematics analysis of the single-finger actuator

The kinematic analysis of the single-finger actuator aims to comprehend the movement behavior and spatial configuration of the soft actuator during operation. The analysis starts by establishing a coordinate system for the actuator and defining its geometric and physical parameters.

As shown in Fig. 3 (a) Cartesian coordinate system is established up with the base of the actuator as the origin. The x-axis is aligned along the length of the actuator, the y-axis is perpendicular to the x-axis in the horizontal plane, and the z-axis is vertically oriented. The bending of the actuator is analyzed by examining the transformation of coordinates along these axes. the bending radius R represents the single-finger actuator's constant curvature bending motion, with the central angle θ corresponding to the actuator's length l.Fig. 3 (b) illustrates the planar view of the single-finger actuator in its bent state. The distance between the arcs $O_{i-1}O_i$ is represented by the distance $\| O_{i-1}O_i\|$ between the upper and lower end faces of the actuator. Geometrically, when the actuator's bending angle is θ the planar displacement trajectory forms an angle of θ /2 with the arc's tangent. The unknown end position of the actuator can be determined using the arc curvature $k$and arc length l as follows:

$$R = \frac{1}{k} \tag{5}$$

$$\theta = l{\cdot}k \tag{6}$$

$$O_{i-1}O_i = 2R{\cdot}sin\left(\frac{\theta}{2}\right) \tag{7}$$

The transformation from the coordinate system O_{i-1} to O_i can be demonstrated in three steps based on geometric relationships:

1. Rotate the rotary axis $\frac{\theta}{2}$ by the O_i-axis of the coordinate system O_{i-1}.
2. Move $O_{i-1}O_i$ along the rotated coordinate system z_{i-1},which is the imaginary path in Fig. 3.
3. Turn $\frac{\theta}{2}$ with the axis of rotation of the moved coordinate system y_{i-1} to obtain the coordinate system O_i.

Treating the soft actuator's movement as constant curvature bending allows us to determine the motion coordinates of characteristic points using the above method. The D-H matrix coordinate transformation

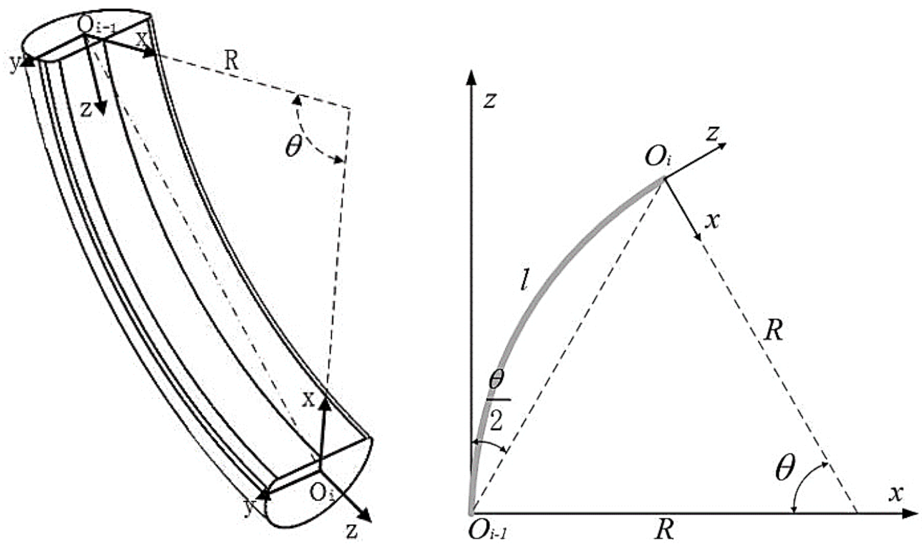

(a) Actuator kinematics modelling in 3D (b) Actuator kinematics modelling plan

Fig. 3. Actuator modelling schematic.

method can then be applied to perform kinematic analysis of the soft actuator. The changes in the prismatic and rotational joints yield the parameters listed in Table 2:

By consecutively multiplying the above three D-H transformation matrices from left to right, the transformation matrix from the upper coordinate system O_{i-1}. to the lower end face coordinate system O_i.of the soft actuator is obtained:

$$T_{i-1}^{i} = R_y(\theta/2)gT_z(Po_{i-1}o_iP)R_y(\theta/2) = \begin{bmatrix} C(kl) & 0 & S(kl) & (1-C(kl))/k \\ 0 & 1 & 0 & 0 \\ -S(kl) & 0 & C(kl) & S(kl)/k \\ 0 & 0 & 0 & 1 \end{bmatrix} \tag{8}$$

Where, $C(kl) = \cos(kl); S(kl) = \sin(kl)$

Calculating the transformation matrix from coordinate system O_i. to coordinate system O_{i-1}' provides the spatial coordinate transformation relationship of the soft actuator, laying the foundation for subsequent work on the soft actuator.

2.2.2. Constitutive model of single-finger actuators

The Yeoh constitutive model is employed to describe the hyperplastic behavior of the silicone material. The model captures the non-linear stress-strain relationship, which is essential for accurately predicting the actuator's deformation under applied pressure. The strain energy density function W. For the Yeoh model is given by:

$$W = C_{10}(I_1-3)^2 + C_{20}(I_1-3)^2 \tag{9}$$

$$I_1 = \lambda_1^2 + \lambda_2^2 + \lambda_3^2 \tag{10}$$

Where, W is the strain energy density function of unidirectional bending of the actuator; λ_1, λ_2 and λ_3 are the principal stretch ratios of the flexible actuator in the axial, circumferential, and radial directions, respectively.

Table 2
D-H Parameters of the Soft Actuator.

Joint	θ	d	a	α
1	$\theta_1 = kl/2$	0	0	$\pi/2$
2	0	$d_2 = 2\sin(kl/2)/2$	0	$-\pi/2$
3	$\theta_3 = kl/2$	0	0	$\pi/2$

2.2.3. Mathematical modelling of single-finger actuators

Flexible actuators have subtle uncertain deformations in the process of deformation produced by air pressure expansion, so based on the use of non-linear properties, the thesis proposes the following constraints:

(1) The elastic material is incompressible;
(2) The inner cavity is rectangular during the motion of the actuator;
(3) the drive constant curvature bending.

As shown in Fig. 4, in the soft body drive by air pressure deformation, full consideration of the wall thickness, the wall of the inner cavity in different directions of the change of the relationship between the equation is:

$$\begin{cases} \lambda_1 = L/L_1 \\ \lambda_2 = \dfrac{1}{2}\cdot\left(\dfrac{b-2t}{B-2t} + \dfrac{h-t_1-t_2}{H-2t}\right) \\ \lambda_3 = \dfrac{1}{4}\cdot\left(\dfrac{t_1}{t} + \dfrac{t_2}{t} + \dfrac{2\cdot t_3}{t}\right) \end{cases} \tag{11}$$

Where, l_1 represents the length of the center axis of the single-finger flexible driver before deformation; the width of the drive before deformation is denoted by $H-2t$; the total width of the drive after deformation is denoted by t, t_1, t_2, $t_3$after the deformation of the wall thickness of the soft drive in different directions, as shown in Fig. 4.

(l_1:Length of the center axis of the single-finger flexible driver before deformation; h: Width of the drive before deformation $H-2t$; t: Total width of the drive after deformation; t_1, t_2, t_3:Wall thickness of the soft drive in different directions after deformation.

e_1:Distance between the bottom surface of the cavity and its center axis when not subjected to external air pressure;e_2 :Distance between the upper layer of the cavity and its center axis when not subjected to external air pressure.)

The soft actuator is bent at constant curvature when inflated to produce bending, which can be introduced from the geometric relationship:{

$$\begin{cases} L = L_1 + e\cdot\theta \\ l_1 = L_1 + (e_1+e_2)\cdot\theta \end{cases} \tag{12}$$

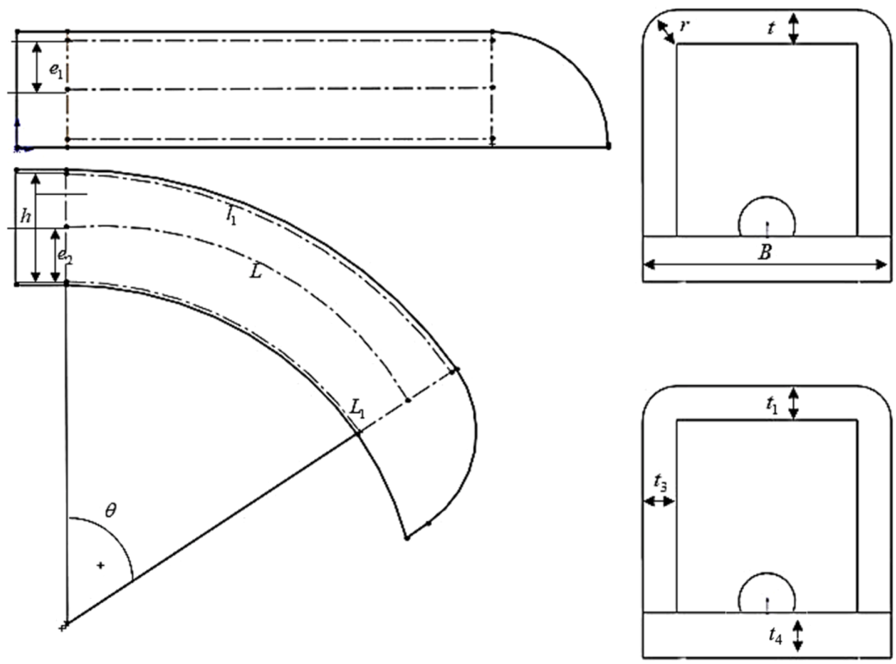

Fig. 4. Actuator size before and after deformation.

$$\begin{cases} t_1 = \dfrac{h}{2} - e_2 \\ t_2 = \left(\dfrac{h}{2} - e_1\right) \\ t_3 = t_4 = t \end{cases} \tag{13}$$

Where, The distance between the bottom surface of the cavity and its center axis when it is not subjected to external air pressure is e_1, and the distance between the upper layer of the cavity and its centre axis when it is not subjected to external air pressure is e_2.

When the flexible actuator is inflated to produce a bending deformation, the paper treats the volume of the flexible material cavity as V_r, and the volume of the air pressure that fills the interior as V_a, so that it is respectively:

$$V_r = S_r L \tag{14}$$

$$V_a = S_a L \tag{15}$$

Where, S_r is the bottom area of the flexible material silicone; S_a is the bottom area of the space occupied by the external fluid-filled cavity. Due to the incompressibility of the silicone, the volume V_r occupied by the flexible driver before deformation and the volume V_{r0} occupied after deformation remain unchanged, the following relationship is obtained:

$$V_r = V_{r0} \tag{16}$$

The width of the cavity before deformation b, and the height of the whole cavity h, can be obtained by Eqs. 11, 12 and 13 as:

$$b = \frac{4-\pi}{2}r - e_1 + \frac{1+2t}{4} + \left(\begin{array}{c} \dfrac{(-2\pi r - 2B - 2H + 8r + \pi t)L_1 t}{2L} + \dfrac{(\pi^2 - 8\pi + 16)r^2}{4} \\ + \left\{ (\pi - 4)re_1 + \dfrac{(3\pi - 12)rt}{2} + \dfrac{9 - 2\pi}{4}t^2 + \dfrac{4-\pi}{4}r + e_1^2 + 3e_1 t - \dfrac{8e_1 + 4t + 1}{16} \right\} \end{array} \right)^{05} \tag{17}$$

$$h = \frac{1}{4}\left\{ \begin{array}{c} (2\pi - 8)^2 r^2 + (16\pi - 64)re_1 + (24\pi - 96)rt + (36 - 8\pi)t^2 + (48t + 8)e_1 \\ -4\pi r + 16{e_1}^2 - 4t + 1 + \dfrac{L_1 t}{L} + [(64 - 16\pi)r + 8\pi t - 16(B + H)] \end{array} \right\}^{0.5} \tag{18}$$

In the absence of an external force, all the work done by the air pressure is converted into bending deformation of the flexible driver, according to the principle of virtual work:

$$PdV_a + V_r dW = 0 \tag{19}$$

$$P\frac{dV_a}{d\theta} + V_r\frac{dW}{d\theta} = 0 \tag{20}$$

$$P = \frac{[-bh + 2e_2(b - 2t) - (\pi - 4)(2rt - t^2)]L\frac{dW}{d\theta}}{2Le_2\frac{db}{d\theta} + [2e_2(b - 2t) + (\pi - 4)(r - t)^2]e_1} \tag{21}$$

By solving Eqs. (11) and (21), Fig. 5 is obtained, which illustrates the relationship between fluid pressure and the bending angle of the soft body actuator. This figure also demonstrates the influence of various factors such as wall thickness and chamber height on the actuator's

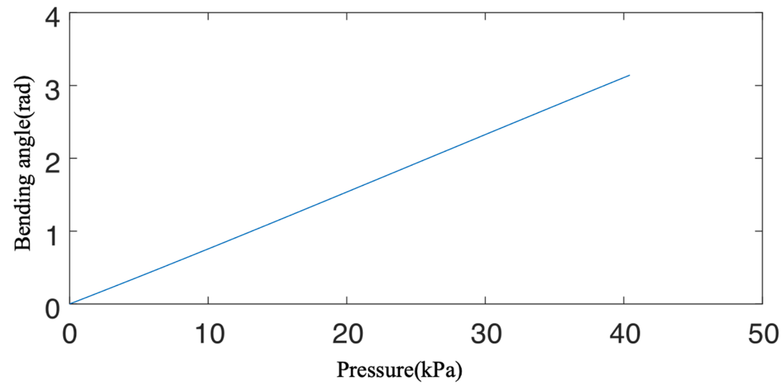

Fig. 5. Connection between pressure and bending angle.

performance. It is evident that the bending angle of the actuator increases linearly with an increase in external air pressure.

3. Single finger actuator Abaqus finite element analysis(FEA)

3.1. Yeoh model parameterization

The Yeoh constitutive model was selected over other material models, such as the Neo-Hookean model, due to its ability to represent the large deformation behavior of hyperplastic materials more accurately like silicone. Unlike the Mooney-Rivlin and Ogden models, which respectively use strain invariants and principal stretch ratios to describe the strain energy, the Yeoh model offers a balanced approach in terms of computational efficiency and accuracy. There are several models with their pros and cons, including Mooney-Rivlin, Ogden, Yeoh, Neo-Hookean, Arruda-Boyce, and Blatz-Ko [65,66]. The choice of the Yeoh model was also informed by its adaptability to the specific properties of the silicone materials used, which exhibit nonlinear behavior that cannot be captured adequately by the Neo-Hookean model.

In the case of hyperplastic materials, the constitutive model provides a means of demonstrating the material properties. The study of the constitutive modelling of flexible actuators is primarily concerned with determining the strain energy density function of the intrinsic model, which is given by the Yeoh model in Eq. (9).

In the research process, the material properties of an object can be determined from the relationship between the force and the deformation of the material. The principal elongation γ_{ij} in the strain energy density function W is deflected to find the principal axial force of the material, which is also known as the stress and Cauchy-Green strain tensor [67], where the principal axial force is expressed as:

$$t_i = \frac{\partial W}{\partial \gamma_i} = \frac{\partial W}{\partial I_1}\frac{\partial I_1}{\partial \gamma_i} + \frac{\partial W}{\partial I_2}\frac{\partial I_2}{\partial \gamma_i} + \frac{\partial W}{\partial I_3}\frac{\partial I_3}{\partial \gamma_i} \tag{22}$$

Substituting Eq. (7) and Eq. (8) into Eq. (22) yields a conversion equation between the spindle force t_i and the main extension ratio λ_i:

$$\begin{cases} t_1 = 2\lambda_1\left[\dfrac{\partial W}{\partial I_1} + (\lambda_2^2+\lambda_3^2)\dfrac{\partial W}{\partial I_2} + (\lambda_2^2\lambda_3^2)\dfrac{\partial W}{\partial I_3}\right] \\ t_2 = 2\lambda_2\left[\dfrac{\partial W}{\partial I_1} + (\lambda_1^2+\lambda_3^2)\dfrac{\partial W}{\partial I_2} + (\lambda_1^2\lambda_3^2)\dfrac{\partial W}{\partial I_3}\right] \\ t_3 = 2\lambda_3\left[\dfrac{\partial W}{\partial I_1} + (\lambda_1^2+\lambda_2^2)\dfrac{\partial W}{\partial I_2} + (\lambda_1^2\lambda_2^2)\dfrac{\partial W}{\partial I_3}\right] \end{cases} \tag{23}$$

Where, t_1, t_2, t_3 are the principal stress ratios in the strain direction [68].

The stress-strain relationship of the material is obtained by performing tensile experiments on the material specimen to determine the material parameters.

In the case of incompressible materials, the third covariate is invariant i.e. exists:

$$I_3 = \lambda_1^2\lambda_2^2\lambda_3^2 = 1 \tag{24}$$

Therefore, in the case of uniaxial tensile experiment, the main elongation ratio can be defined as:

$${\lambda_2}^2 = {\lambda_3}^2 = \frac{1}{\lambda_1} \tag{25}$$

The joint Eq. (8), Eq. (23) and Eq. (25) can be obtained as the relationship between the elongation ratio and the invariants:

$$I_1 = \lambda_1^2 + \frac{2}{\lambda_1} \tag{26}$$

In addition, the conversion relationship between principal stress and principal elongation ratio is given by:

$$t_1 = \frac{2}{\lambda_1}\left(\lambda_1^2 - \frac{1}{\lambda_1^2\lambda_2^2}\right)\left(\frac{\partial W}{\partial I_1} + {\lambda_2}^2\frac{\partial W}{\partial I_2}\right) \tag{27}$$

Finally, the strain energy density function of the Yeoh model, Eq. (9) is brought into the above equation and combined with Eq. (24) and Eq. (27) can be derived:

$$\frac{t_1}{2(\lambda_1 - 1/\lambda_1^2)} = C_{10} - 6C_{20} + 2C_{20}(\lambda_1^2 + 2/\lambda_1) \tag{28}$$

Eq. (28) reveal the connection between the stress-strain of the silica gel material used in the thesis and the unknown content parameters C_{10} and C_{20} of the Yeoh-model species. Firstly, the stress values corresponding to the material at each moment in the state of different stretch ratios are derived from the tensile experiments; then, a right-angled coordinate system is established with the experimentally derived values, i.e., $2(\lambda_1^2 + 2/\lambda_1)$, $t_1/2(\lambda_1 - 1/\lambda_1^2)$, as the horizontal and vertical coordinates, and the scatter plots are depicted in the coordinate system. Then, by virtue of the primary function, the scatter plot is fitted with a primary function, and the resulting slope can be regarded as the unknown parameter C_{20} of the material in the A model, and the parameter C_{10} can be found by converting the resulting function with the intercept $(C_{10} - 6 \cdot C_{20})$ of the y-axis. Therefore, the unknown parameters of the model, can be derived from this.

Table 3
Properties of E series Silicones.

Model	E600	E605	E610	E615
Hardness/HA	0	5	10	15
Elongation/%	300	400	400	400
Mixing Ratio	1:1	1:1	1:1	1:1
Cure time/h	3–5h	3–5h	3–5h	3–5h
Work time/min	20–40	20–40	20–40	20–40

Table 4
Properties of Ecoflex series silicones.

Model	Ecoflex5	Ecoflex00–50	Ecoflex00–30	Ecoflex00–33
Hardness/HA	5	00–50	00–30	00–33
Elongation/%	1000%	980%	900%	900%
Mixing Ratio	1:1	1:1	1:1	1:1
Cure time/h	3–5h	3–5h	3–5h	3–5h
Work time/min	20–40	20–40	20–40	20–40

3.2. Silicone material selection and related parameter determination

In Tables 3 and 4, it is observed that E600 has low elongation, while Ecoflex 00–50 demonstrates better elongation with a certain degree of hardness. Additionally, the shrinkage of both materials is less than 0.1%, which is negligible and thus meets the constraints of the model established in this thesis. Based on these properties, T00 silicone is selected as the upper elastic material for the soft actuator, and E600 silicone is chosen as the lower elastic material.

To determine the material parameters in the strain energy density function of the model, it is essential to conduct experiments on rubber samples to obtain the stress-strain relationship. Uniaxial tensile tests are performed to collect the necessary experimental data. As illustrated in Fig. 6, the HD-B609B-S electro-hydraulic servo tensile testing machine is utilized for this purpose, showcasing the specimen mold and the tensile testing process.

Data on the tensile stress and deformation of the rubber samples are collected, as shown in Fig. 7. The stress-strain relationship of the rubber samples is further analyzed by converting the measured stress-deformation data into stress-strain data using the appropriate Eq. (29):

$$\lambda = \frac{l + \Delta l}{l} \tag{29}$$

Where, l is the original length of the rubber sample and Δl is the deformation length.

The averaged data were further processed and the obtained scatter plots were fitted with one linear function using MATLAB, from which the unknown parameters of the Yeoh eigenmodal were derived.

A linear function was fitted using the function$y_1 = 0.0076x + 0.0681$ with $y_2 = 0.081x + 0.741$ According to the slope and intercept of the fitted function, the unknown parameters C_{10}, C_{20} in the Yeoh model can be obtained, i.e., C_{10}=0.1MPa and C_{20}=0.0076MPa for the lower silicone material of the finger of the soft driver and C_{10}=0.08MPa and C_{20}=0.015MPa for the upper silicone material of the finger of the driver. The above parameters can be applied in Abaqus simulation.

3.3. Abaqus finite element modeling

3.3.1. Single finger sactuator Abaqus finite element modeling

The 3D model of the finger designed in SolidWorks was imported into Abaqus and entered into the simulation process, setting the parameters of the upper silicone material as C_{10}=0.08MPa, C_{20}=0.015MPa, =0 and the lower silicone material as C_{10}=0.1MPa, C_{20}=0.0076MPa, C_{30}=0.

In this section, the stress distribution cloud maps of the inner wall and inner cavity of the proposed wave-shaped contour single-finger actuator under different pressures are analyzed using Abaqus simulation. Additionally, the impact of various structural parameters on the bending performance of the single-finger actuator is examined.

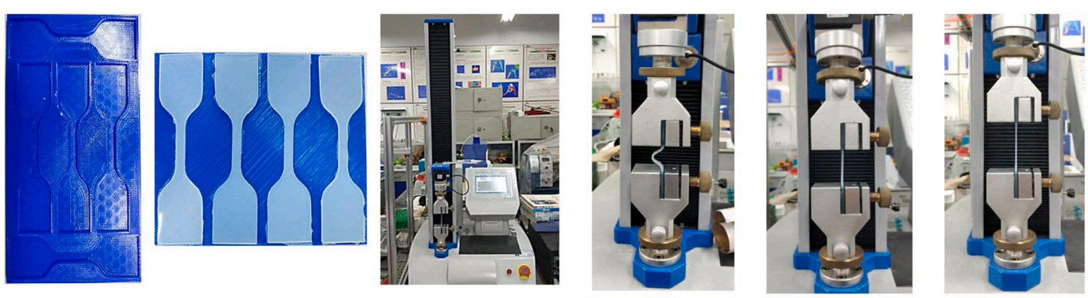

Fig. 6. Sample tensile testing machine experimental process.

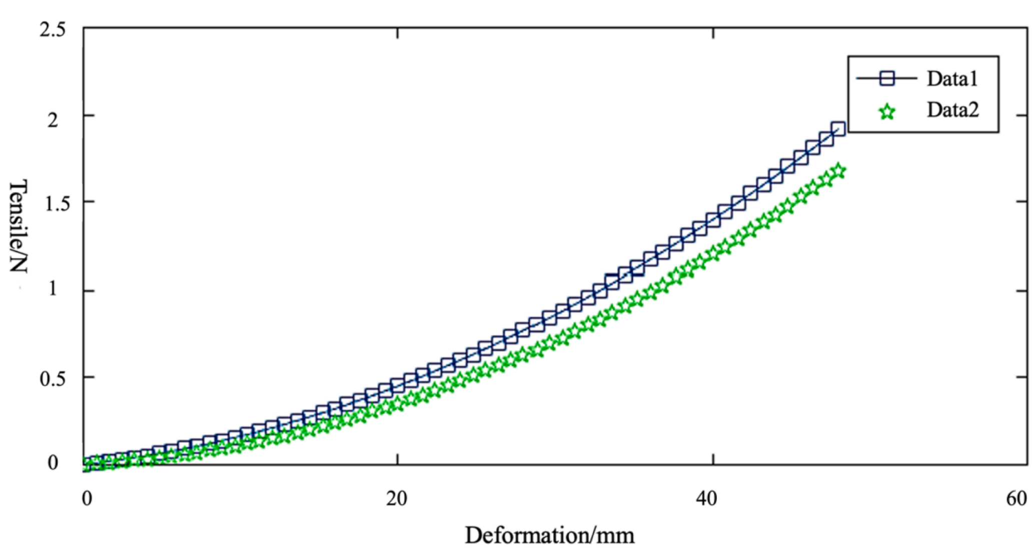

Fig. 7. Stress-strain relationship of rubber specimen.

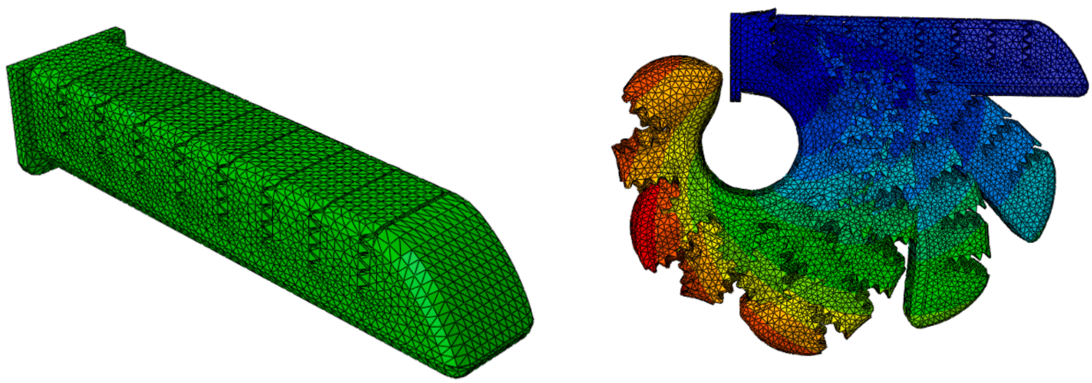

Fig. 8. FEM model of actuator.

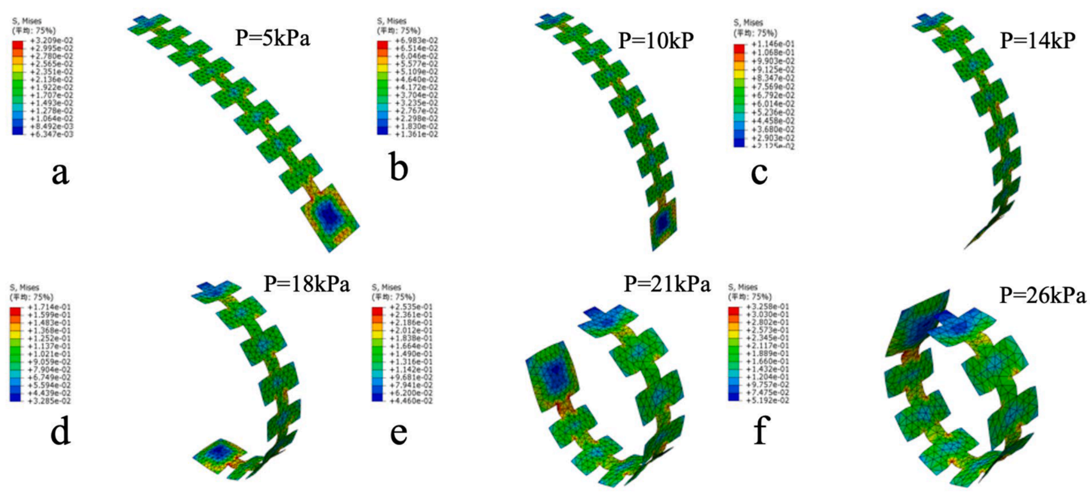

Fig. 9. Actuator's bottom of inner cavity bending state and stress distribution in the FEA model at different pressure.

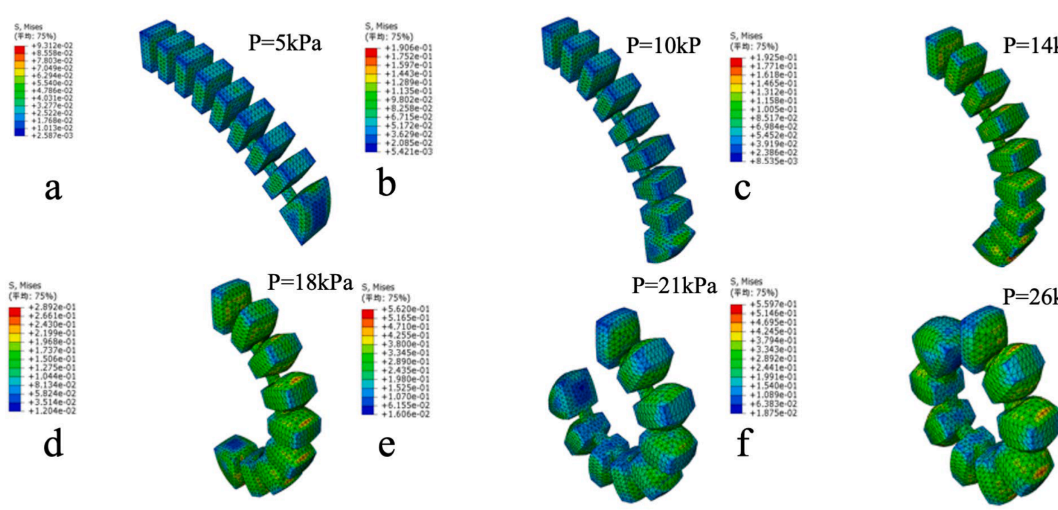

Fig. 10. Actuator's inner cavity bending state and stress distribution in the FEA model at different pressure.

Fig. 8 illustrates the finite element model and the actuator's deformation under linearly increasing pressure. As the pressure increases, the deformation of adjacent chambers from the base to the fingertip progressively intensifies. Consequently, the bending degree increases, leading to a decrease in the radius of curvature.

Figs. 9 and 10 display the stress distribution within the actuator's inner cavity and the bottom of the inner cavity at different pressures (5 kPa, 10 kPa, 14 kPa, 18 kPa, 21 kPa, and 26 kPa). At 26 kPa, the actuator achieves a 180° bend, characterized by the maximum bending angle and minimum radius of curvature. The maximum stress is observed at the fingertip end of the inner cavity bottom during bending. At lower pressures, the maximum stress on the constraint layer is less than that on

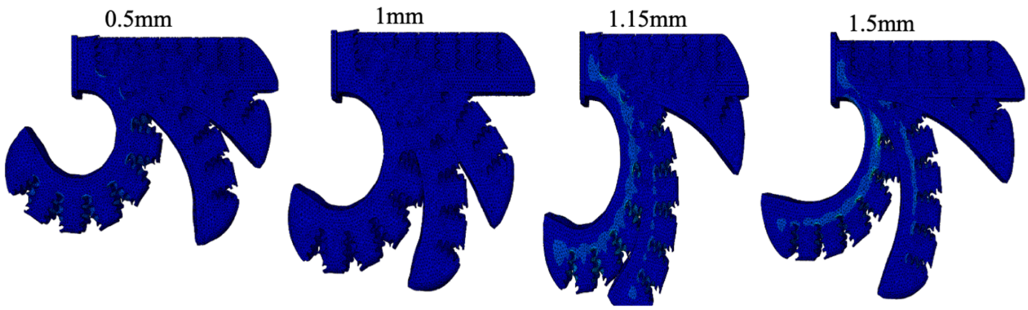

Fig. 11. Actuator wall thicknesses 0.5mm, 1mm, 1.15mm, 1.5mm, bending simulation in FEA model.

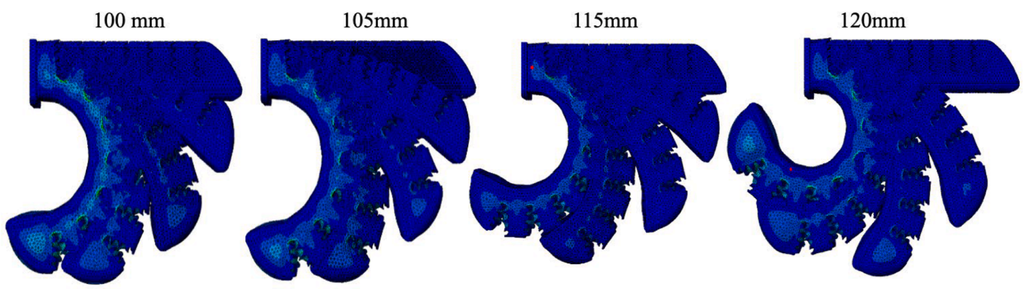

Fig. 12. Actuator Length 100mm, 105mm, 115mm, 120mm bending simulation in FEA model.

the inner cavity surface. However, at higher pressures, the maximum stress on both the inner cavity surface and the constraint layer becomes similar and concentrated, with nearly equal values.

3.3.2. Structural parameters influence on actuator

3.3.2.1. Wall thickness. The variation in wall thickness significantly impacts the bending performance and durability of soft actuators. In this study, the effects of wall thicknesses of 0.5 mm, 1 mm, 1.15 mm, and 1.3 mm were analyzed using Abaqus simulations. A linearly increasing pressure was applied to the inner cavity, and the bending angles at pressures of 5 kPa, 10 kPa, 14 kPa, and 21 kPa were recorded. As shown in Fig. 4-17, the bending angle decreases as wall thickness increases. This negative correlation arises because thicker sidewalls require more energy to bend due to their increased stiffness.

The simulations indicate that a wall thickness of 1 mm provides optimal bending performance, striking a balance between flexibility and structural integrity. Therefore, a wall thickness of 1 mm was selected for the soft actuator design (Figs. 11 and 12).

3.3.2.2. Finger length. Finger lengths of 100 mm, 105 mm, 115 mm, and 120 mm were analyzed. The results indicated a positive correlation between finger length and bending angle under the same pressure. Longer fingers improved bending performance but reduced structural rigidity and gripping force. A finger length of 115mm was selected as it balances bending performance and gripping stability.

3.3.2.3. Constraint layer thickness. For the constraint layer thickness, tests were conducted on thicknesses of 2 mm, 3 mm, 4 mm, and 5 mm. Increasing the thickness reduced the bending angle, showing a negative correlation, as shown in Fig. 13. A 2mm constraint layer, despite good bending performance, caused undesirable expansion at the fingertip. A thickness of 3mm was found to be optimal, providing structural support while maintaining good bending performance.

These analyses highlight the importance of optimizing structural parameters to achieve balanced bending performance, ensuring the effectiveness of the soft actuator in various applications. the optimal structural parameters were determined to be: a wall thickness of 1.5mm, a finger length of 115mm, and a constraint layer thickness of 3mm.

3.4. Comparative analysis of fingertip output force

A fingertip output force simulation was conducted to compare the wave-shaped contour actuator with the traditional FPN soft actuator. The simulation was performed using Abaqus, with a flat plate positioned 50 mm below each actuator. A linearly increasing input pressure was applied to both actuators to observe their performance. As shown in Figs. 14 and 15, the wave-shaped contour actuator demonstrated a 40% increase in fingertip contact force compared to the traditional FPN actuator, reaching its peak at 60 kPa. This enhancement is attributed to

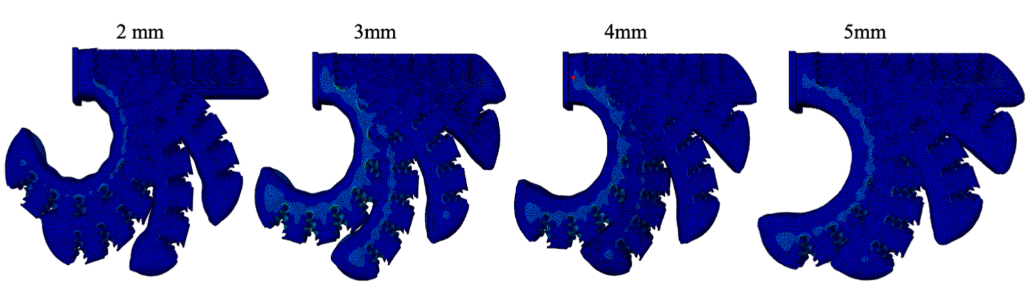

Fig. 13. Actuator restriction layer thickness 2mm, 3mm, 4mm, 5mm, bending simulation in FEA model.

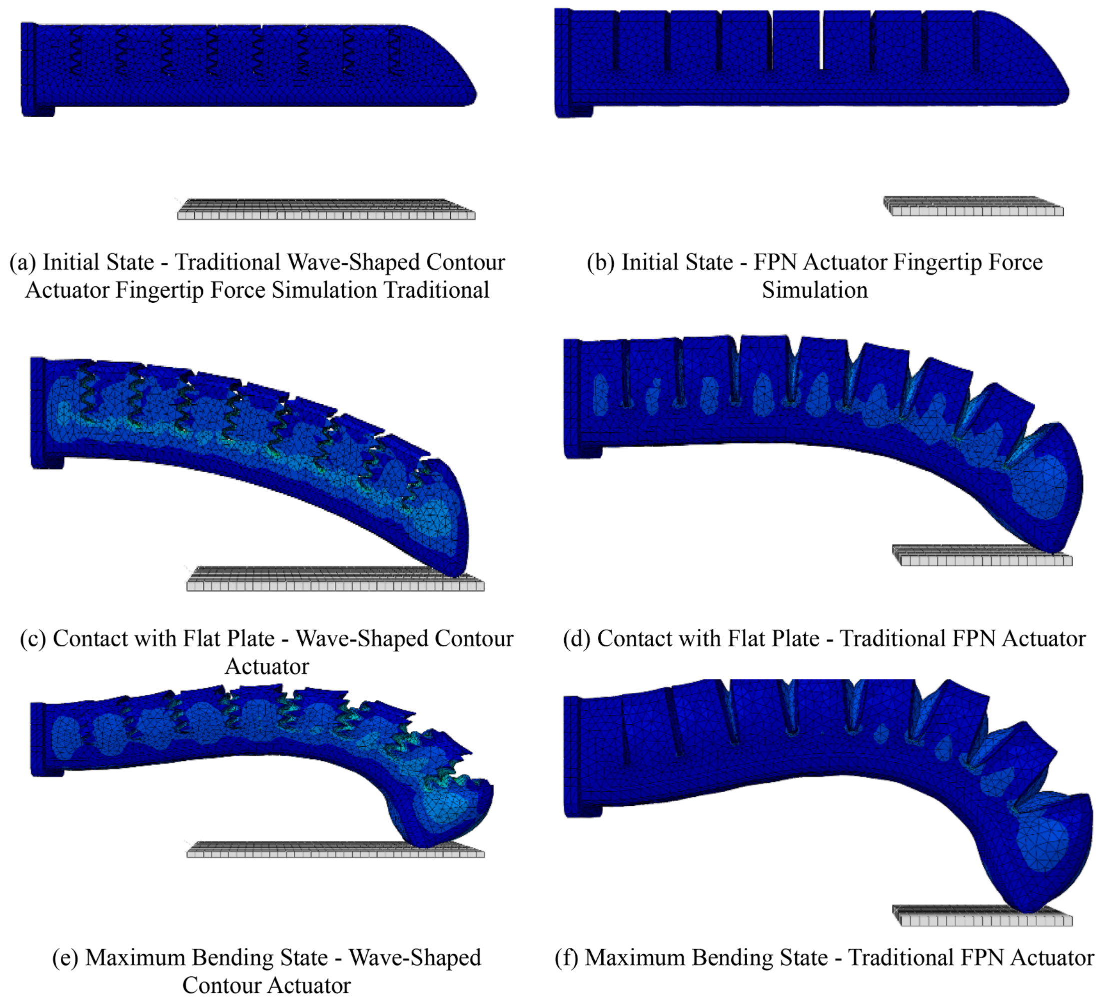

(a) Initial State - Traditional Wave-Shaped Contour Actuator Fingertip Force Simulation Traditional

(b) Initial State - FPN Actuator Fingertip Force Simulation

(c) Contact with Flat Plate - Wave-Shaped Contour Actuator

(d) Contact with Flat Plate - Traditional FPN Actuator

(e) Maximum Bending State - Wave-Shaped Contour Actuator

(f) Maximum Bending State - Traditional FPN Actuator

Fig. 14. Comparative simulation of fingertip output force for traditional FPN and wave-shaped contour actuators.

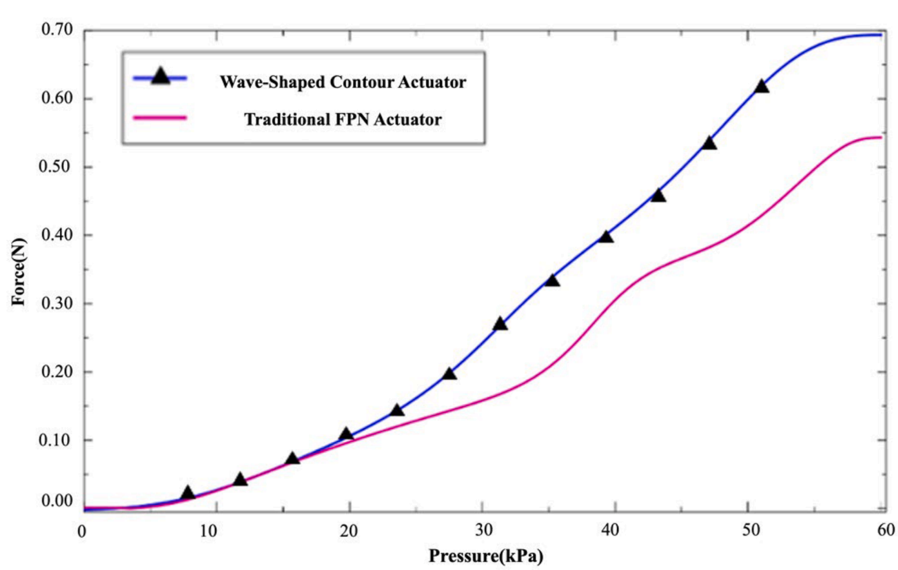

Fig. 15. Fingertip output force vs. Pressure for traditional FPN and wave-shaped contour actuators.

the wave-shaped contour's improved sidewall engagement, ensuring smooth interaction between adjacent chambers, and preventing deadlocking.

As shown in Fig. 14, the wave-shaped contour actuator demonstrates significant improvements in fingertip force when compared to the traditional FPN actuator. Specifically, when subjected to a linearly increasing pressure of up to 60 kPa, the wave-shaped actuator achieves a 40% higher fingertip force. This enhancement is primarily due to the improved sidewall engagement and effective interaction between chambers, as depicted in Fig. 14 (e) and (f). The performance difference is further illustrated in Fig. 15, where the force vs. pressure relationship is clearly demonstrated, showing the superior force generation capability of the wave-shaped design.

The wave-shaped contour actuator shows significant improvements over the traditional FPN structure in terms of fingertip contact force. The results indicate that, as input pressure increases from 5 kPa to 60 kPa, the wave-shaped contour actuator consistently generates higher contact force compared to the FPN actuator. This improvement is due to the wave-shaped contour's ability to engage sidewalls more effectively, maintaining stable contact between chambers and enhancing overall actuator rigidity. The unique design prevents interference and ensures consistent contact throughout the bending motion, thereby increasing the effectiveness of the grasping force.

As depicted in Fig. 15, the relationship between input pressure and output force for both the traditional FPN and wave-shaped contour actuators is clearly demonstrated. The wave-shaped contour actuator consistently generates a higher output force across the pressure range, with the force reaching a peak of approximately 0.65 N at 60 kPa compared to the traditional FPN actuator's peak of 0.45 N. This performance difference highlights the superior efficiency of the wave-shaped contour actuator, which benefits from enhanced sidewall engagement and optimized force transmission. The graph also indicates that the wave-shaped actuator achieves greater force at lower pressure levels, making it advantageous for applications requiring efficient energy use.

The wave-shaped contour actuator's ability to generate higher contact forces while maintaining flexibility represents a significant advancement in soft robotics. This dual improvement in rigidity and adaptability makes the proposed actuator suitable for applications in industrial automation and service robotics, where robust and flexible grasping is essential. The simulation results validate the design's efficacy and demonstrate its potential for broader use in scenarios requiring enhanced force generation without additional structural complexity.

4. Experimental results and discussion

In this chapter, the experimental design, results, and discussion are presented to validate the performance of the wave-shaped contour single-finger actuator. The experiments focus on bending performance and grasping capability under various conditions.

4.1. Materials and setup

The experiments utilize T00 silicone for the upper elastic layer and E600 silicone for the lower elastic layer of the actuator. The actuator's geometric parameters are set as follows: wall thickness of 1mm, finger length of 115mm, and constraint layer thickness of 3mm. The process is shown in the Fig. 16, The soft actuator mold proposed in the paper was completed by 3D printing with the UltimakerS5–3D printer model.

4.2. Bending performance trajectory analysis

The bending angles observed at different pressures are shown in Fig. 17. The results demonstrate that the bending angle increases with applied pressure, following a linear trend. This confirms the theoretical predictions and simulation results.

Fig. 18(a) shows the end trajectory of the soft actuator under linearly increasing pressure from the pneumatic system, ranging from 0° to 168° This trajectory is compared with the constant curvature bending model and the Abaqus finite element model in Fig. 18(b) and (c).

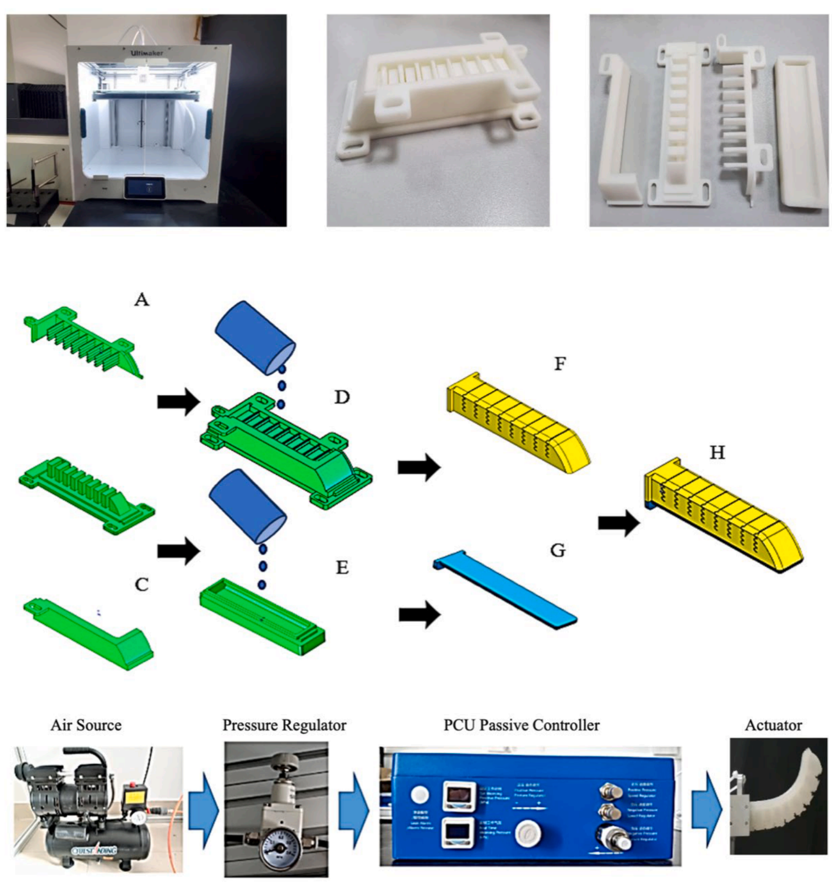

Fig. 16. Single Finger Actuator Fabrication Process.

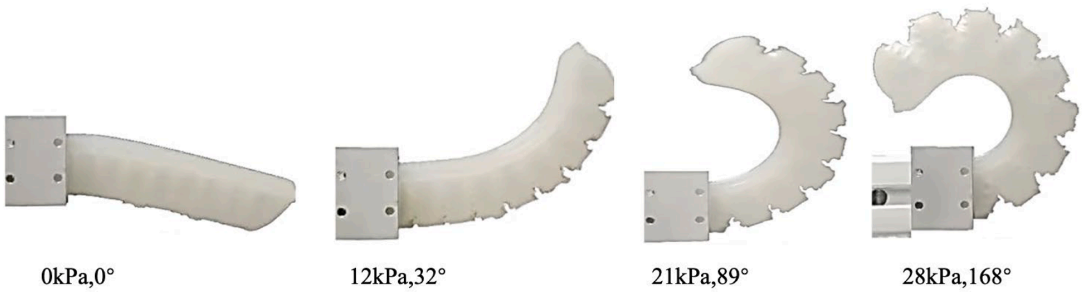

Fig. 17. Bending diagrams at different air pressures.

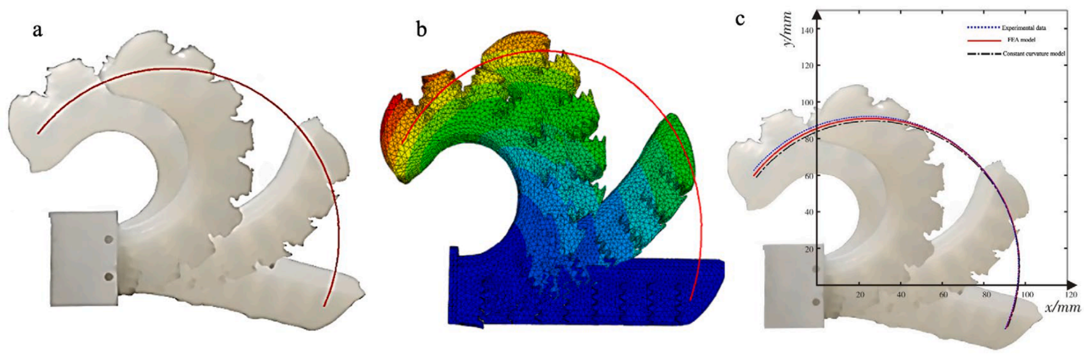

Fig. 18. Single-finger drive trajectory (a) Actual Motion Trajectory (b) FEA Motion Trajectory (c) Actual and FEA motion Trajectory.

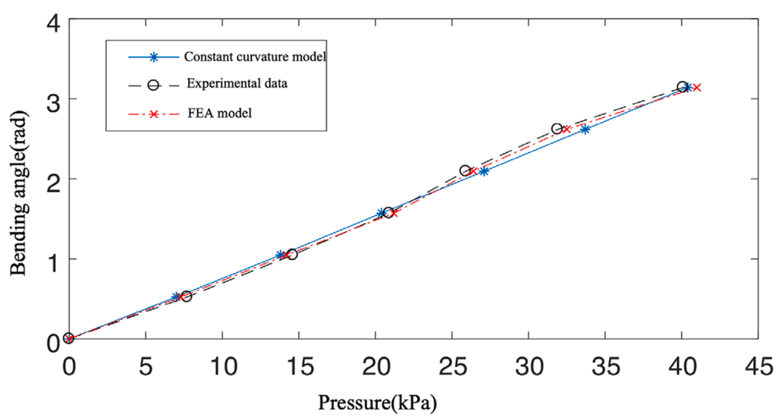

Fig. 19. The link between pressure and bending angle under different models (mathematical models, experimental data, FEA model).

To quantify the error between the actuator's end trajectory and the theoretical model, Eq. (30) is used. The position error e_i and the root mean square error (RMSE) $e_s$are calculated. The maximum position error for the constant curvature bending model is 4.682mm, with an RMSE of 0.962mm. For the Abaqus FEA model, the maximum position error is 1.753mm, with an RMSE of 1.148mm. Given the actuator length of 115mm, the error for the constant curvature model is within 2%, indicating excellent predictive accuracy and consistency for both models.

$$\begin{cases} e_i = \sqrt{(x_i - x_i')^2 + (y_i - y_i')^2} \\ e_s = \sqrt{\dfrac{\sum_{i=1}^{N} (x_i - x_i')^2 + (y_i - y_i')^2}{N}} \end{cases} \tag{30}$$

In the established Cartesian coordinate system for the actuator's motion plane, the$x$ and y coordinates at any given time during the motion are represented by x_i and $y_i$for the constant curvature and Abaqus models, x_i' and y_i' for the experimental data.

Fig. 19 illustrates the relationship between pressure and bending angle for the single-finger actuator. The experimental data aligns closely with both the constant curvature bending model and the Abaqus FEA model. The data indicates that the wave-shaped contour actuator provides consistent force even at higher bending angles, which is a significant advantage over traditional FPN actuators that may lose efficiency under increased deformation. This confirms that both models accurately predict the actuator's bending performance, validating the correctness of the theoretical and simulation models.

This performance characteristic is crucial for applications involving precision gripping and adaptable force control in complex environments.

The primary sources of error in the experimental and simulation results for the single-finger actuator are as follows:

- Initial Position Under Gravity, the actuator's fingertip starts from a position influenced by gravity, not a perfectly horizontal position. In

Table 5
Dimensions of different objects for grasping.

No.	Name	Weight(g)	Dimensions(cm)
1	Orange	192	Diameter:11
2	Rectangular A	201	6*4*4
3	Drink Can	165	16*14*10
4	Water Bottle	23	21*6*6
5	Cube	64	5*5*5
6	Irregular object	81	28*10*5
7	Jar	36	16*50*80
8	Tissue Box	168	13*6*10
9	Thermos	212	18*7*7
10	Rectangular B	156	20*20*6
11	Rectangular C	174	23*13*6

contrast, the simulation assumes the actuator starts from a horizontal position, leading to discrepancies in the initial conditions.

- Model Assumptions: Both the constant curvature model and the finite element model assume idealized conditions, such as perfect material homogeneity and isotropy. In reality, material inconsistencies and minor defects can cause deviations.
- Material Property Fitting Errors: The parameters C_{10} an C_{20} used in the Abaqus simulations are derived from experimental data using a tensile testing machine and fitted using linear regression, introducing some errors.

4.3. Grasping experiments for irregular objects

As discussed earlier, the variable stiffness soft actuator exhibits excellent elastic deformation capabilities. By selecting appropriate silicone materials for injection molding, the soft fingers achieve a certain hardness. This enables the proposed four-finger pneumatic soft robotic hand to demonstrate effective grasping and flexible coverage for various irregularly shaped objects listed in Table 5.

The four-finger soft robotic hand, as shown in Fig. 20, was fixed in place and tested with 11 different everyday objects of varying shapes and weights. The results demonstrated its strong adaptability and outstanding grasping capabilities.

The experiments demonstrated that the four-finger soft robotic hand could effectively grasp a wide range of objects with varying shapes and sizes. Key observations include:

- The hand could grasp spherical objects like oranges without causing surface damage.
- It provided stable grips on common household items such as water bottles, thermos flasks, and drink cans, regardless of their shape.
- Smooth-surfaced objects like Rubik's cubes and boxes were securely enveloped.
- It successfully grasped flexible objects such as tissue boxes and hollow jars.
- Large, irregular objects were also stably held.
- By adjusting the position of the arc-shaped movable link, the hand could achieve variable stroke grasps, showing excellent versatility

The results indicate that the proposed four-finger soft robotic hand is highly adaptable and practical. It demonstrated excellent enveloping and stability for objects like thermos flasks, Rubik's cubes, and water bottles from various angles.

5. Conclusion

This study presents a four-finger pneumatic soft robotic hand with wave-shaped contour actuators optimized for both bending performance and versatile grasping capabilities. The actuators, designed with selected silicone materials and optimized structural parameters, were successfully fabricated, and tested using a low-cost 3D printing process. Through FEM simulations and experimental validation, it was demonstrated that the actuators achieve a consistent and reliable bending motion, with excellent adaptability to a wide range of object shapes and sizes. The soft robotic hand effectively grasps various everyday items, showcasing its potential for practical applications in industrial automation and daily life.

Comparative experiments have demonstrated that the wave-shaped contour actuator significantly outperforms traditional FPN actuators in terms of grasping adaptability and stability. Specifically, when subjected to various grasping tasks involving objects of irregular geometries, the proposed actuator maintained a more consistent and stable grip compared to conventional designs. The unique geometry of the wave-shaped contour ensures that the actuator can conform more effectively to complex surfaces, thereby enhancing contact stability and improving overall grasping efficiency. Moreover, the experimental results show that the wave-shaped contour actuator achieves a substantial improvement in fingertip contact force and consistency, particularly under

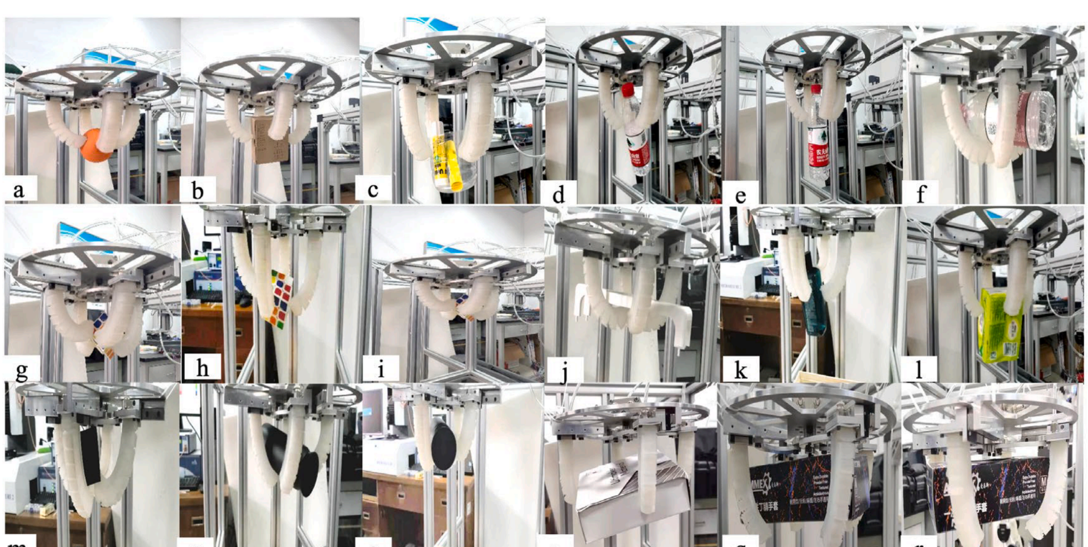

Fig. 20. (a)Orange(b)Rectangular box(c)Drink can(d)Water bottle Posture 1(e)Water bottle Posture 2 (f)Water bottle Posture 3(g)Cube Posture 1 (h)Cube Posture 2 (i)Cube Posture 3(j)irregular object (k)Can (l)Tissue (m) Thermos posture 1 (n) Thermos posture 2 (o) Thermos posture 3 (p) Rectangular B (q) Rectangular C angle 1 (r) Rectangular C angle 2.

varying pressure inputs. This is a significant advancement over traditional FPN actuators, which often exhibit reduced force generation at higher bending angles. The wave-shaped contour actuator exhibited significant improvements in force generation across a wide range of pressure inputs, from 5 kPa to 60 kPa. This consistency in force output and adaptability under different pressure conditions makes the actuator highly suitable for real-world applications, such as service robotics, rehabilitation devices, and industrial automation. The enhanced sidewall engagement ensures stable and reliable performance, even under varying operational pressures, which is crucial for precise and adaptable manipulation tasks.

While our experimental setup validates the reliability and versatility of the actuator, it is acknowledged that further research is needed to explore its performance in extreme conditions, such as high-speed grasping, varying ambient temperatures, and different material properties. Future work will focus on optimizing material selection to improve the environmental resilience of the actuator and expanding the scope of experiments to validate performance in more complex scenarios. Future research will aim to integrate advanced control algorithms to enhance the performance of the soft robotic hand in challenging environments.

The analysis confirms the robustness of the theoretical models and the reliability of the design. Future work will involve refining the actuator design, exploring additional applications, and integrating advanced control algorithms to enhance the performance of the soft robotic hand. The promising results indicate that this design can be a significant advancement in the field of soft robotics, paving the way for innovative solutions in adaptive grippers, robotic hands, and related applications.

CRediT authorship contribution statement

Hui Chen: Conceptualization, Formal analysis, Methodology, Software, Visualization, Validation, Writing – original draft, Writing – review & editing. **Mohammed A.H. Ali:** Methodology, Investigation, Supervision, Funding acquisition, Writing – review & editing. **Zhenya Wang:** Supervision, Writing – review & editing, Funding acquisition. **Junlong Chen:** Writing – review & editing, Formal analysis. **Montaser N.A. Ramadan:** Software, Writing – review & editing, Funding acquisition. **Mohammad Alkhedher:** Methodology, Writing – review & editing, Funding acquisition.

Declaration of competing interest

The authors declare that they have no known competing financial interests or personal relationships that could have appeared to influence the work reported in this paper.

Acknowledgments

The authors would like to acknowledge the financial support from Abu Dhabi University's Office of Research and Sponsored Programs with Grant ID: 19300889. The authors also gratefully acknowledge the financial support of Grant: the Postdoctoral Fellowship Program of China Postdoctoral Science Foundation (Grant No. GZC20231284); the China Postdoctoral Science Foundation (Grant No. 2024M751643).

Data availability

No data was used for the research described in the article.

References

[1] P. Polygerinos, N. Correll, S.A. Morin, B. Mosadegh, C.D. Onal, K. Petersen, M. Cianchetti, M.T. Tolley, R.F. Shepherd, Soft Robotics: Review of Fluid-Driven Intrinsically Soft Devices; Manufacturing, Sensing, Control, and Applications in Human-Robot Interaction, (n.d.). https://doi.org/10.1002/adem.201700016.

[2] F. Ahmed, M. Waqas, B. Jawed, A.M. Soomro, S. Kumar, A. Hina, U. Khan, K. H. Kim, K.H. Choi, Decade of bio-inspired soft robots: a review, Smart Mater. Struct. 31 (2022) 073002, https://doi.org/10.1088/1361-665X/ac6e15.

[3] M. Cianchetti, C. Laschi, A. Menciassi, P. Dario, Biomedical applications of soft robotics, Nat. Rev. Mater. 3 (2018) 143–153, https://doi.org/10.1038/s41578-018-0022-y.

[4] J. Shintake, V. Cacucciolo, D. Floreano, H. Shea, Soft robotic grippers, Adv. Mater. 30 (2018) 1707035, https://doi.org/10.1002/adma.201707035.

[5] A. Zolfagharian, M. Lakhi, S. Ranjbar, Y. Tadesse, M. Bodaghi, 3D printing non-assembly compliant joints for soft robotics, Results Eng. 15 (2022) 100558, https://doi.org/10.1016/j.rineng.2022.100558.

[6] J. Hussan K S, M.P. Subramaniam, M. Kenz K T, P. Sreeram, S. Parvathi, S. Ps, A. Pullanchiyodan, D.M. Mulhivill, P. Raghavan, Fabrication and challenges of 3D printed sensors for biomedical applications-comprehensive review, Results Eng. 21 (2024) 101867, https://doi.org/10.1016/j.rineng.2024.101867.

[7] M. Simić, G.M. Stojanović, Wearable device for personalized EMG feedback-based treatments, Results Eng. 23 (2024) 102472, https://doi.org/10.1016/j.rineng.2024.102472.

[8] S. Qureshi, M. Hanif, V. Jeoti, G.M. Stojanović, M.T. Khan, Review of fabrication of SAW sensors on flexible substrates: challenges and future, Results Eng. 22 (2024) 102323, https://doi.org/10.1016/j.rineng.2024.102323.

[9] F. Amin, A. Waris, J. Iqbal, S.O. Gilani, M.Z. Ur Rehman, S. Mushtaq, N.B. Khan, M. I. Khan, M. Jameel, N. Tamam, Maximizing stroke recovery with advanced technologies: A comprehensive assessment of robot-assisted, EMG-Controlled robotics, virtual reality, and mirror therapy interventions, Results Eng. 21 (2024) 101725, https://doi.org/10.1016/j.rineng.2023.101725.

[10] D. Kulic, E.A. Croft, Affective state estimation for human–robot interaction, IEEE Trans. Robot. 23 (2007) 991–1000, https://doi.org/10.1109/TRO.2007.904899.

[11] C. Sirithunge, H. Wang, F. Iida, Soft touchless sensors and touchless sensing for soft robots, Front. Robot. AI 11 (2024) 1224216, https://doi.org/10.3389/frobt.2024.1224216.

[12] K. Severinson-Eklundh, A. Green, H. Hüttenrauch, Social and collaborative aspects of interaction with a service robot, Rob. Auton. Syst. 42 (2003) 223–234, https://doi.org/10.1016/S0921-8890(02)00377-9.

[13] C. Han, M. Yu, H. Pan, J. Yu, About the design of a new bionic robot with four legs for competition, in: MATEC Web of Conferences, EDP Sciences, 2021, p. 03003, https://doi.org/10.1051/matecconf/202133603003.

[14] M.A. Devi, G. Udupa, P. Sreedharan, A novel underactuated multi-fingered soft robotic hand for prosthetic application, Rob. Auton. Syst. 100 (2018) 267–277, https://doi.org/10.1016/j.robot.2017.11.005.

[15] T. Deng, H. Wang, W. Chen, X. Wang, R. Pfeifer, Development of a new cable-driven soft robot for cardiac ablation, in: 2013 IEEE International Conference on Robotics and Biomimetics (ROBIO), IEEE, 2013, pp. 728–733, https://doi.org/10.1109/ROBIO.2013.6739547.

[16] J.M. Krahn, F. Fabbro, C. Menon, A soft-touch gripper for grasping delicate objects, IEEE/ASME Trans. Mechatronics 22 (2017) 1276–1286, https://doi.org/10.1109/TMECH.2017.2663322.

[17] M. Calisti, A. Arienti, M.E. Giannaccini, M. Follador, M. Giorelli, M. Cianchetti, B. Mazzolai, C. Laschi, P. Dario, Study and fabrication of bioinspired octopus arm mockups tested on a multipurpose platform, in: 2010 3rd IEEE RAS & EMBS International Conference on Biomedical Robotics and Biomechatronics, IEEE, 2010, pp. 461–466, https://doi.org/10.1109/BIOROB.2010.5625959.

[18] M. Cianchetti, T. Ranzani, G. Gerboni, T. Nanayakkara, K. Althoefer, P. Dasgupta, A. Menciassi, Soft robotics technologies to address shortcomings in today's minimally invasive surgery: the STIFF-FLOP approach, Soft. Robot. 1 (2014) 122–131, https://doi.org/10.1089/soro.2014.0001.

[19] F. Schmitt, O. Piccin, L. Barbé, B. Bayle, Soft robots manufacturing: a review, Front. Robot. AI. 5 (2018) 84, https://doi.org/10.3389/frobt.2018.00084.

[20] A. Petcu, M. Georgescu, D. Tarniţă, Actuation systems of active orthoses used for gait rehabilitation, Appl. Mech. Mater. 880 (2018) 118–123, https://doi.org/10.4028/www.scientific.net/AMM.880.118.

[21] L.G. Machado, M.A. Savi, Medical applications of shape memory alloys, Braz. J. Med. Biol. Res. 36 (2003) 683–691, https://doi.org/10.1590/S0100-879x2003000600001.

[22] T. Peng, J. Lan, P. Lu, C. Deng, Z.-Y. Zhao, Y.-Z. Wang, High-Performance biobased elastomers with both high strength and high toughness, ACS Appl. Polym. Mater. 6 (2024) 4204–4214, https://doi.org/10.1021/acsapm.4c00290.

[23] Y. Gao, L. Sun, P. Chen, Y. Wu, Y. Liu, C. Gao, A stretch hardening self-assembly strategy inspired by natural rubber for degradable, recyclable and self-repairing polyurethane elastomers, Polym. Degrad. Stab. 215 (2023) 110441.

[24] S. Wang, X. Chen, L. Guo, S. Wang, F. Dong, H. Liu, X. Xu, A human muscle-inspired, high strength, good elastic recoverability, room-temperature self-healing, and recyclable polyurethane elastomer based on dynamic bonds, Compos. Sci. Technol. 248 (2024) 110457.

[25] W. Zhao, Z. Zhang, J. Hu, X. Feng, J. Xu, Y. Wu, S. Yan, Robust and ultra-fast self-healing elastomers with hierarchically anisotropic structures and used for wearable sensors, Chem. Eng. J. 446 (2022) 137305.

[26] O. Nazarova, V. Osadchyy, T. Hutsol, S. Glowacki, T. Nurek, V. Hulevskyi, I. Horetska, Mechatronic automatic control system of electropneumatic manipulator, Sci. Rep. 14 (2024) 6970.

[27] H. Yang, G. Wei, L. Ren, A novel soft actuator: MISA and its application on the biomimetic robotic arm, IEEe Robot. Autom. Lett. 8 (2023) 2373–2380.

[28] S. Kashef Tabrizian, F. Cedric, S. Terryn, B. Vanderborght, SMA wire use in hybrid twisting and bending/extending soft fiber-reinforced actuators, in: Actuators, MDPI, 2024, p. 125. https://www.mdpi.com/2076-0825/13/4/125. accessed October 26, 2024.

[29] X. Chen, L. Gong, L. Wei, S.-C. Yeh, L.Da Xu, L. Zheng, Z. Zou, A wearable hand rehabilitation system with soft gloves, IEEe Trans. Industr. Inform. 17 (2020) 943–952.
[30] M. Sui, Y. Ouyang, H. Jin, Z. Chai, C. Wei, J. Li, M. Xu, W. Li, L. Wang, S. Zhang, A soft-packaged and portable rehabilitation glove capable of closed-loop fine motor skills, Nat. Mach. Intell. 5 (2023) 1149–1160, https://doi.org/10.1038/s42256-023-00728-z.
[31] P. Dhatrak, J. Durge, R.K. Dwivedi, H.K. Pradhan, S. Kolke, Interactive design and challenges on exoskeleton performance for upper-limb rehabilitation: a comprehensive review, Int. J. Interact. Des. Manuf. (2024), https://doi.org/10.1007/s12008-024-02090-9.
[32] Z. Zhang, A. Calderon, X. Huang, A. Huang, Research status and prospect of finger rehabilitation machinery, MDER 17 (2024) 1–22, https://doi.org/10.2147/MDER.S429206.
[33] E. Rogers, P. Polygerinos, C. Walsh, E. Goldfield, Smart and connected actuated mobile and sensing suit to encourage motion in developmentally delayed infants, J. Med. Device 9 (2015) 030914, https://doi.org/10.1115/1.4030550.
[34] R. Mutlu, G. Alici, M.In Het Panhuis, G.M. Spinks, 3D printed flexure hinges for soft monolithic prosthetic fingers, Soft. Robot. 3 (2016) 120–133, https://doi.org/10.1089/soro.2016.0026.
[35] A.A. Stokes, R.F. Shepherd, S.A. Morin, F. Ilievski, G.M. Whitesides, A hybrid combining hard and soft robots, Soft Robot. 1 (2014) 70–74, https://doi.org/10.1089/soro.2013.0002.
[36] K.-J. Cho, J.-S. Koh, S. Kim, W.-S. Chu, Y. Hong, S.-H. Ahn, Review of manufacturing processes for soft biomimetic robots, Int. J. Precis. Eng. Manuf. 10 (2009) 171–181, https://doi.org/10.1007/s12541-009-0064-6.
[37] B.S. Homberg, R.K. Katzschmann, M.R. Dogar, D. Rus, Haptic identification of objects using a modular soft robotic gripper, in: 2015 IEEE/RSJ International Conference on Intelligent Robots and Systems (IROS), IEEE, 2015, pp. 1698–1705, https://doi.org/10.1109/IROS.2015.7353596.
[38] C. Choi, W. Schwarting, J. DelPreto, D. Rus, Learning object grasping for soft robot hands, IEEE Robot. Autom. Lett. 3 (2018) 2370–2377, https://doi.org/10.1109/LRA.2018.2810544.
[39] Z. Xie, A.G. Domel, N. An, C. Green, Z. Gong, T. Wang, E.M. Knubben, J.C. Weaver, K. Bertoldi, L. Wen, Octopus arm-inspired tapered soft actuators with suckers for improved grasping, Soft. Robot. 7 (2020) 639–648, https://doi.org/10.1089/soro.2019.0082.
[40] C. Tawk, H. Zhou, E. Sariyildiz, M.In Het Panhuis, G.M. Spinks, G. Alici, Design, modeling, and control of a 3D printed monolithic soft robotic finger with embedded pneumatic sensing chambers, IEEE/ASME Trans. Mechatron. 26 (2021) 876–887, https://doi.org/10.1109/TMECH.2020.3009365.
[41] Morphological Transformation between Flat and Tube Structures by Coordinated Motions of Soft Pneumatic Microactuators | Scientific Reports, (n.d.). https://www.nature.com/articles/s41598-019-50670-7 (accessed July 31, 2024).
[42] D. Al-Shamkhani, F. Al-Farhan, A. Al-Ibadi, The wearable foot rehabilitation soft robot, in: 2021 International Conference on Communication & Information Technology (ICICT), IEEE, 2021, pp. 197–201, https://doi.org/10.1109/ICICT52195.2021.9568432.
[43] W. Hu, G. Alici, Bioinspired Three-Dimensional-Printed Helical Soft Pneumatic Actuators and Their Characterization, https://Home.Liebertpub.Com/Soro (2020). https://doi.org/10.1089/soro.2019.0015.
[44] Design and testing of a soft parallel robot based on pneumatic artificial muscles for wrist rehabilitation | Scientific Reports, (n.d.). https://www.nature.com/articles/s41598-020-80411-0 (accessed July 31, 2024).
[45] A. O'Halloran, F. O'Malley, P. McHugh, A review on dielectric elastomer actuators, technology, applications, and challenges, J. Appl. Phys. 104 (2008) 071101, https://doi.org/10.1063/1.2981642.
[46] Y. Miao, W. Dong, Z. Du, Design of a soft robot with multiple motion patterns using soft pneumatic actuators, IOP Conf. Ser.: Mater. Sci. Eng. 269 (2017) 012013, https://doi.org/10.1088/1757-899X/269/1/012013.
[47] W. Wang, Y. Tang, C. Li, Controlling bending deformation of a shape memory alloy-based soft planar gripper to grip deformable objects, Int. J. Mech. Sci. 193 (2021) 106181, https://doi.org/10.1016/j.ijmecsci.2020.106181.
[48] Dynamical analysis and development of a biologically inspired SMA caterpillar robot - IOPscience, (n.d.). https://iopscience.iop.org/article/10.1088/1748-3190/aa8472 (accessed July 31, 2024).
[49] Y. Hao, S. Biswas, E.W. Hawkes, T. Wang, M. Zhu, L. Wen, Y. Visell, A Multimodal, Enveloping soft gripper: shape conformation, bioinspired adhesion, and expansion-driven suction, IEEE Trans. Robot. 37 (2021) 350–362, https://doi.org/10.1109/TRO.2020.3021427.
[50] A. Zolfagharian, L. Durran, S. Gharaie, B. Rolfe, A. Kaynak, M. Bodaghi, 4D printing soft robots guided by machine learning and finite element models, Sens. Actuators A 328 (2021) 112774, https://doi.org/10.1016/j.sna.2021.112774.
[51] D.S. Shah, J.P. Powers, L.G. Tilton, S. Kriegman, J. Bongard, R. Kramer-Bottiglio, A soft robot that adapts to environments through shape change, Nat. Mach. Intell. 3 (2021) 51–59, https://doi.org/10.1038/s42256-020-00263-1.
[52] A.K. Dickerson, P.G. Shankles, N.M. Madhavan, D.L. Hu, Mosquitoes survive raindrop collisions by virtue of their low mass, Proc. Natl. Acad. Sci. 109 (2012) 9822–9827, https://doi.org/10.1073/pnas.1205446109.
[53] Y. Qiu, E. Zhang, R. Plamthottam, Q. Pei, Dielectric elastomer artificial muscle: materials innovations and device explorations, Acc. Chem. Res. 52 (2019) 316–325, https://doi.org/10.1021/acs.accounts.8b00516.
[54] N. Wang, B. Chen, H. Guo, C. Cui, X. Zhang, Design of dielectric elastomer grippers using Bezier curves, Mech. Mach. Theory. 158 (2021) 104216, https://doi.org/10.1016/j.mechmachtheory.2020.104216.
[55] R.F. Shepherd, A.A. Stokes, J. Freake, J. Barber, P.W. Snyder, A.D. Mazzeo, L. Cademartiri, S.A. Morin, G.M. Whitesides, Using explosions to power a soft robot, Angew. Chem. Int. Ed. 52 (2013) 2892–2896, https://doi.org/10.1002/anie.201209540.
[56] J. Li, Y. Pi, Fuzzy time delay algorithms for position control of soft robot actuated by shape memory alloy, Int. J. Control Autom. Syst. 19 (2021) 2203–2212, https://doi.org/10.1007/s12555-018-0313-5.
[57] S.J. Park, C.H. Park, Suit-type wearable robot powered by shape-memory-alloy-based fabric muscle, Sci. Rep. 9 (2019) 9157.
[58] C. Christianson, C. Bayag, G. Li, S. Jadhav, A. Giri, C. Agba, T. Li, M.T. Tolley, Jellyfish-Inspired soft robot driven by fluid electrode dielectric organic robotic actuators, Front. Robot. AI 6 (2019), https://doi.org/10.3389/frobt.2019.00126.
[59] M. Franke, A. Ehrenhofer, S. Lahiri, E.-F. Henke, T. Wallmersperger, A. Richter, Dielectric elastomer actuator driven soft robotic structures with bioinspired skeletal and muscular reinforcement, Front. Robot. AI. 7 (2020) 510757, https://doi.org/10.3389/frobt.2020.510757.
[60] Y.-Y. Xiao, Z.-C. Jiang, Y. Zhao, Liquid Crystal Polymer-Based Soft Robots, (n.d.). https://doi.org/10.1002/aisy.202000148.
[61] G.Z. Lum, Z. Ye, X. Dong, H. Marvi, O. Erin, W. Hu, M. Sitti, Shape-programmable magnetic soft matter, Proc. Natl. Acad. Sci. USA (2016) 113, https://doi.org/10.1073/pnas.1608193113.
[62] Y. Ju, R. Hu, Y. Xie, J. Yao, X. Li, Y. Lv, X. Han, Q. Cao, L. Li, Reconfigurable magnetic soft robots with multimodal locomotion, Nano Energy 87 (2021) 106169, https://doi.org/10.1016/j.nanoen.2021.106169.
[63] J. Li, L. Zu, G. Zhong, M. He, H. Yin, Y. Tan, Stiffness characteristics of soft finger with embedded SMA fibers, Compos. Struct. 160 (2017) 758–764, https://doi.org/10.1016/j.compstruct.2016.10.045.
[64] H. Rodrigue, W. Wang, D.-R. Kim, S.-H. Ahn, Curved shape memory alloy-based soft actuators and application to soft gripper, Compos. Struct. 176 (2017) 398–406, https://doi.org/10.1016/j.compstruct.2017.05.056.
[65] A. Zolfagharian, M.A.P. Mahmud, S. Gharaie, M. Bodaghi, A.Z. Kouzani, A. Kaynak, 3D/4D-printed bending-type soft pneumatic actuators: fabrication, modelling, and control, Virtual. Phys. Prototyp. 15 (2020) 373–402, https://doi.org/10.1080/17452759.2020.1795209.
[66] M. Bodaghi, A. Serjouei, A. Zolfagharian, M. Fotouhi, H. Rahman, D. Durand, Reversible energy absorbing meta-sandwiches by FDM 4D printing, Int. J. Mech. Sci. 173 (2020) 105451, https://doi.org/10.1016/j.ijmecsci.2020.105451.
[67] A. Alibakhshi, A. Imam, S.E. Haghighi, Effect of the second invariant of the Cauchy–Green deformation tensor on the local dynamics of dielectric elastomers, Int. J. Non. Linear. Mech. 137 (2021) 103807, https://doi.org/10.1016/j.ijnonlinmec.2021.103807.
[68] S. Wacharawichanant, P. Opasakornwong, R. Poohoi, M. Phankokkruad, Influence of cellulose fiber content on morphology and properties of poly(lactic acid)/propylene-ethylene copolymer/cellulose composites, Solid State Phenomena 315 (2021) 128–133, https://doi.org/10.4028/www.scientific.net/SSP.315.128.